Supplementary Information for

Ultrafast laser processing of silk films by bulging and ablation for optical functional devices

Ming Qiao[1], Huimin Wang[2], Heng Guo[1], Ma Luo[1], Yuzhi Zhao[1], Haoze Han[1], Jianfeng Yan[1]*, and Yingying Zhang[2]

1. State Key Laboratory of Tribology in Advanced Equipment, Department of Mechanical Engineering, Tsinghua University, Beijing 100084, China
2. Key Laboratory of Organic Optoelectronics and Molecular Engineering of the Ministry of Education, Department of Chemistry, Tsinghua University, Beijing 100084, China
*Corresponding author.
Email: yanjianfeng@tsinghua.edu.cn

This PDF file includes:
Figure S1 to S17
Table S1 to S2

Other supporting materials for this manuscript include the following:
Movie S1

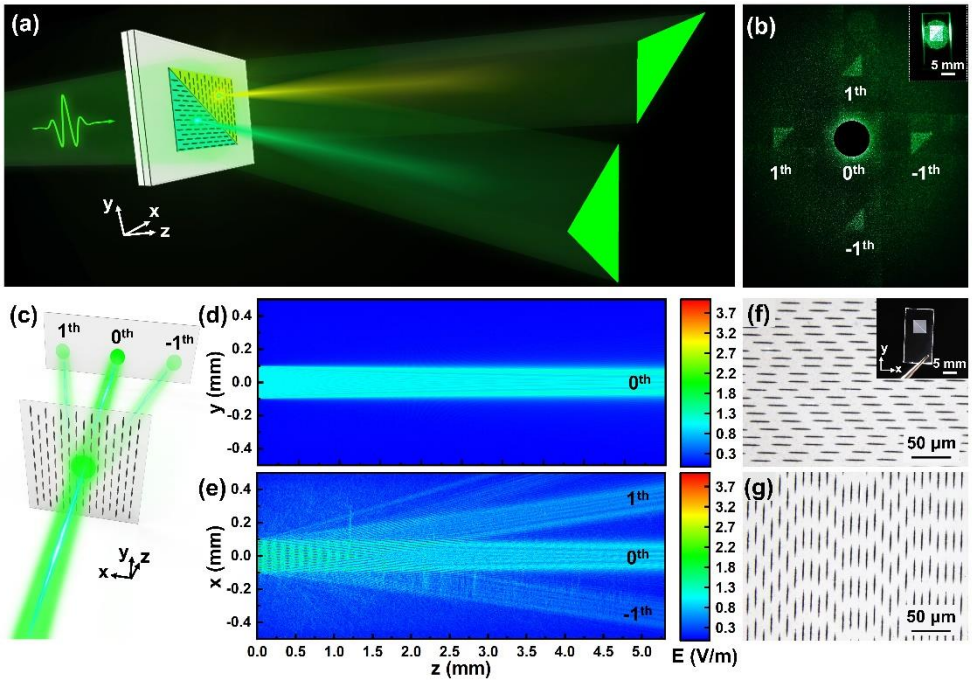

Figure S1. (a) Schematic illustration of an optical device based on the silk film. (b) Diffraction pattern of the optical device (inset: photograph of the device being irradiated with a 530 nm illumination laser). (c) Schematic of the diffraction effects when a laser passes through a silk film containing periodic strip-shaped structures. Simulated light fields behind the silk film in (d) y-z and (e) x-z planes. (f) Optical micrograph of a strip-shaped structural array (horizontal) processed with an ultrafast laser (inset: photograph of the device). (g) Optical micrographs of a strip-shaped structural array (vertical) processed with an ultrafast laser.

Figure S1a shows a schematic of a square device that can be utilized for optical encryption. The device consists of two triangular regions with periodic strip-shaped structures parallel to x- and y-axes. **Figure S1f** and **S1g** show the microscopic images of the strip-shaped structures in the two triangular regions. When illuminated with a 530 nm laser, the square-shaped device projects triangular patterns onto the screen owing to diffraction effects (**Movie S1**). The first-order diffraction pattern of the device is presented in **Figure S1b**. The inset shows the device irradiated with a 530 nm laser, where one triangular pattern in the horizontal direction and another in the vertical direction can be observed. The zero-order diffraction pattern was blocked using a light barrier. The second and higher orders diffraction patterns were blocked by an iris. **Figure S1c** shows a schematic of the diffraction effect of the illumination laser passing through a silk film with periodic strip-shaped structures. The zero-order diffracted light propagated in the original direction, whereas the first-order diffracted light was deflected to the sides. The

plane defined by the diffracted light (x-z plane) was perpendicular to the direction of the strip-shaped structures.

Further, the optical field distribution of the illumination laser behind the silk film was simulated, as illustrated in **Figure S1d** and **S1e**. A plane wave was used as the illumination laser for simulation. **Figure S1d** shows that the illumination laser did not deflect in the plane parallel to the strip-shaped structures (y-z plane). Owing to diffraction effects, the illumination laser was split into multiple beams and deflected in different directions in the plane perpendicular to the strip-shaped structures (x-z plane), as shown in **Figure S1e**. The simulation results are consistent with the experimental findings. This device demonstrates potential for optical encryption. The triangle represents the encrypted information that can be decrypted from a square pattern. Using this optical encryption method, more complex patterns can be encrypted by patterning strip-shaped structural arrays using an ultrafast laser. The areas of interference information can be patterned with strip-shaped structural arrays that are perpendicular to the strip-shaped structures in the areas of encrypted information. When an optical encryption device is illuminated with a laser, the encrypted information and interference information are projected in different directions.

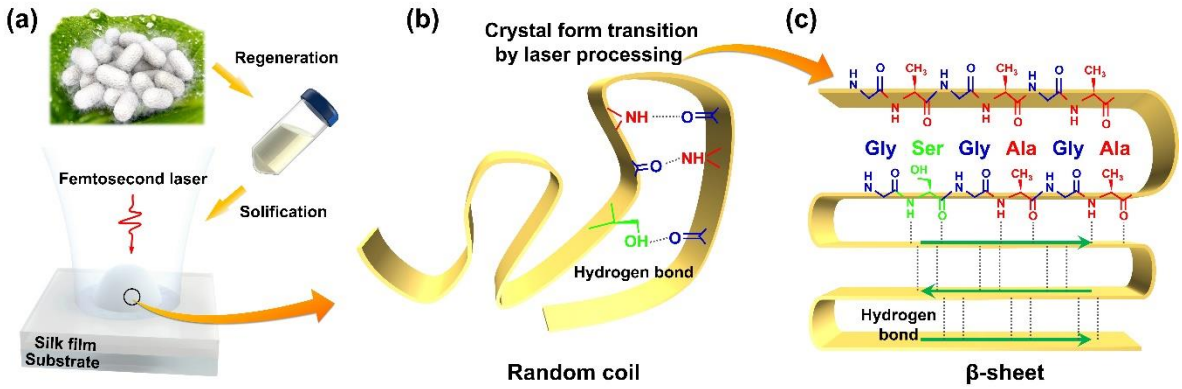

Figure S2. (a) Schematic of the silk film preparation process and bulge processing. (b-c) Schematic illustration of the crystal form transition of silk proteins through laser processing.

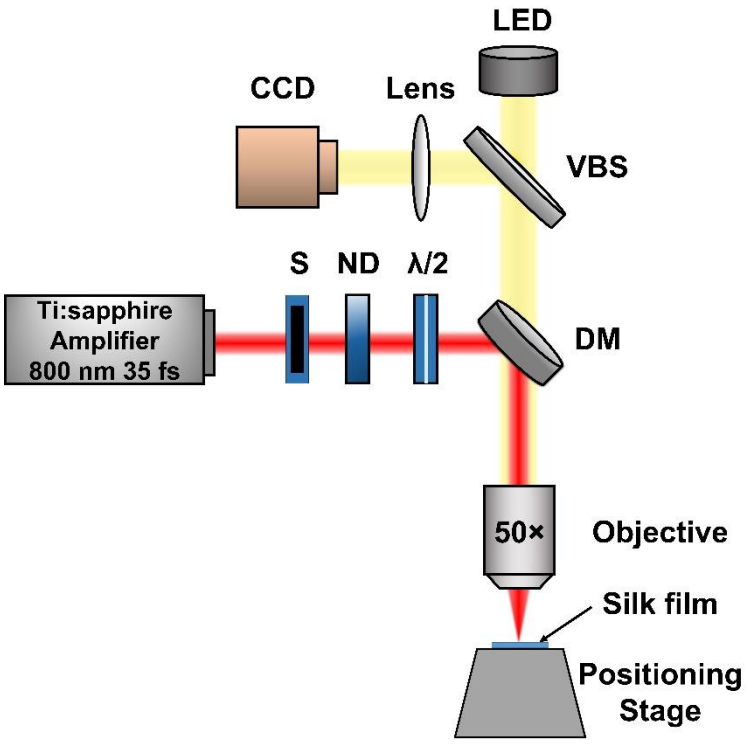

Figure S3. Experimental setup for silk film processing using a femtosecond laser. S (shutter); ND (neutral-density filter); λ/2 (half-wave plate); DM (dichroic mirror); VBS (visible light beam splitter); CCD (charge-coupled device camera).

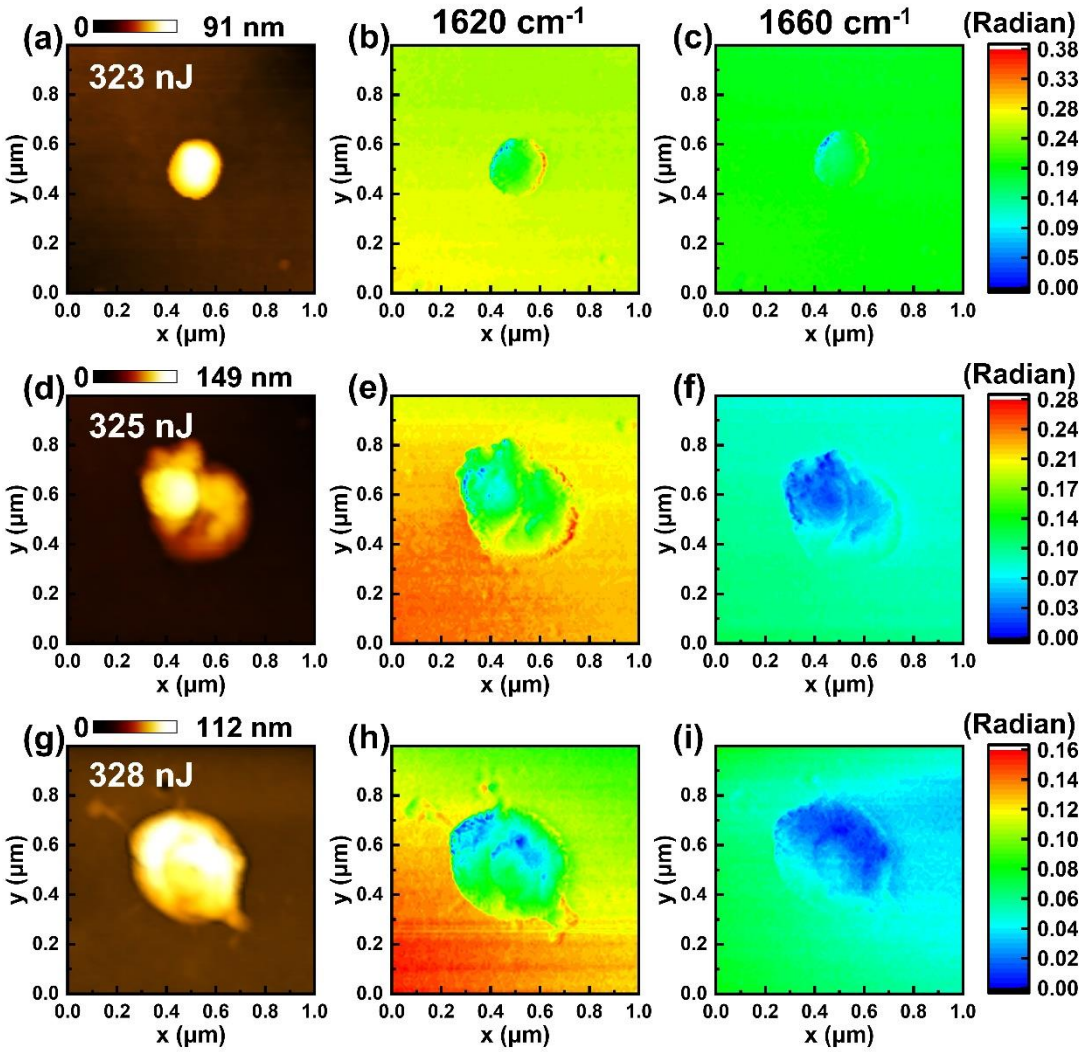

Figure S4. AFM and nano-IR phase images of bulges generated using laser pulses with pulse energies ranging from 323 to 328 nJ.

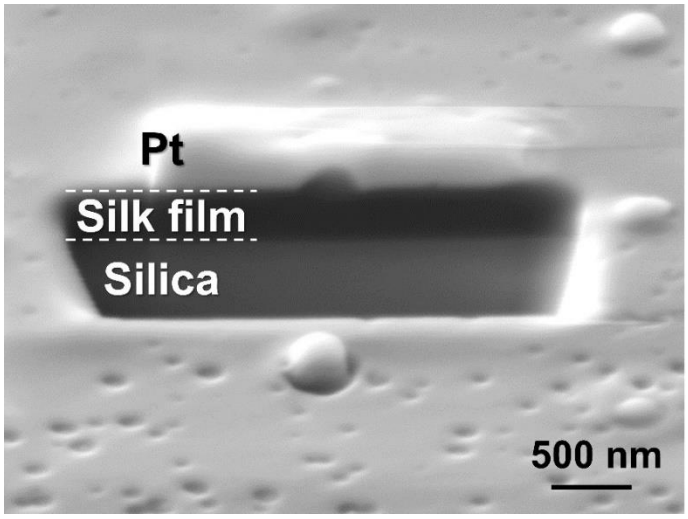

Figure S5. Cross-sectional SEM image of a bulge processed with an ultrafast laser.

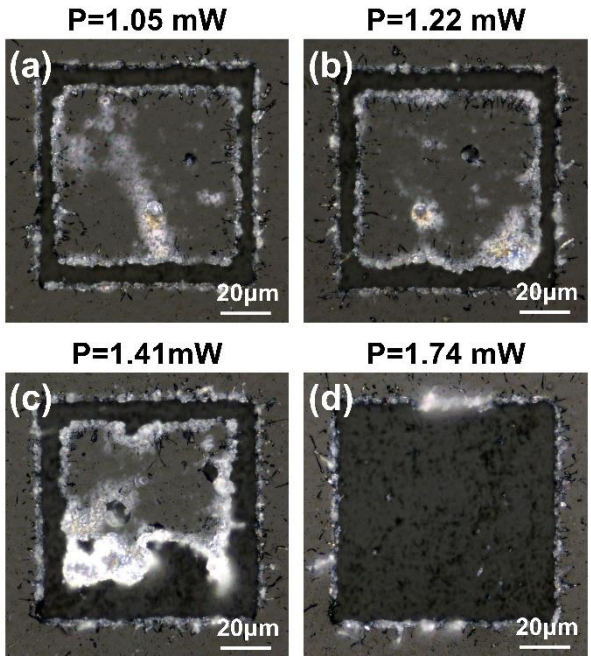

Figure S6. The optical microscopy images of silk films processed with ultrafast lasers at power levels ranging from 1.05 mW to 1.74 mW.

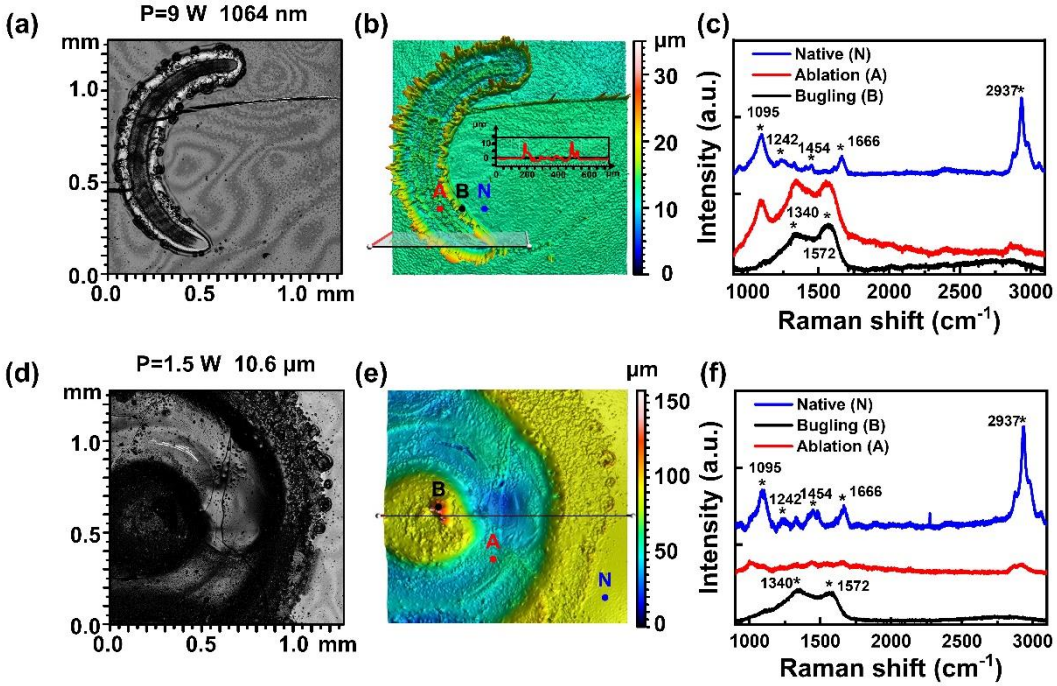

Figure S7. The processing of silk film using long pulse lasers. (a) The optical microscopy image, (b) confocal image, and (c) Raman spectra of a silk film processed using a nanosecond laser (1064 nm) with a power of 9 W. (d) The optical microscopy image, (e) confocal image, and (f) Raman spectra of a silk film processed using a CO_2 laser (10.6 μm) with a power of 1.5 W.

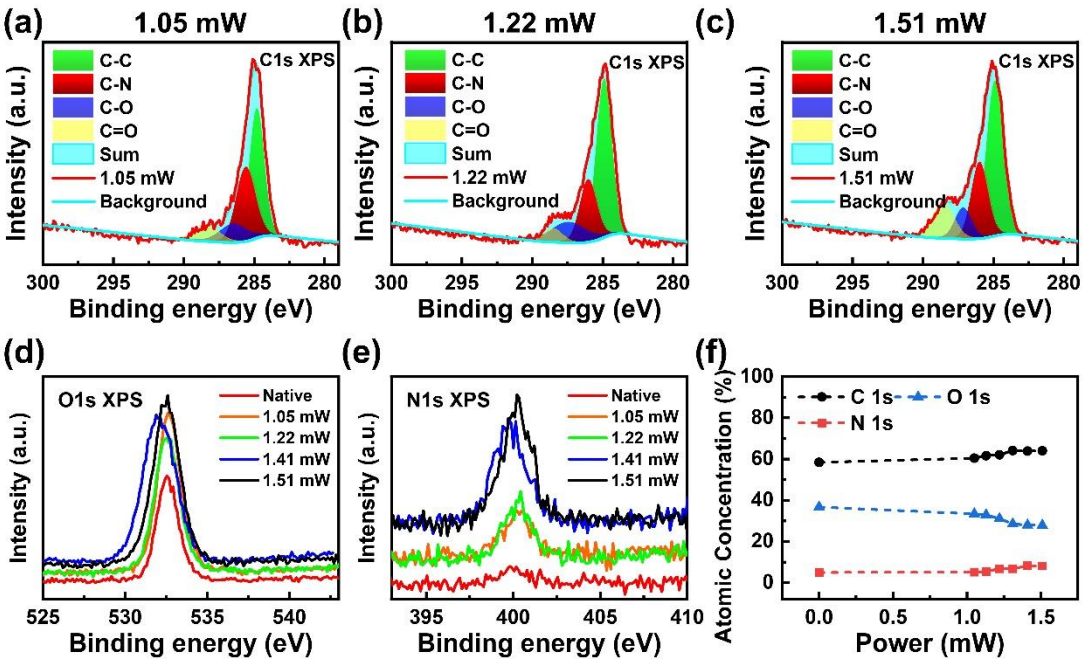

Figure S8. XPS analysis of a silk film before and after ultrafast laser processing. (a-c) High-resolution XPS C1s spectra of silk film processed by an ultrafast laser with powers ranging from 1.05 mW to 1.51 mW. High-resolution XPS (d) O1s spectra and (e) N1s spectra of of silk film before and after processing with an ultrafast laser. (f) The atomic concentrations of carbon, oxygen, and nitrogen before and after laser processing.

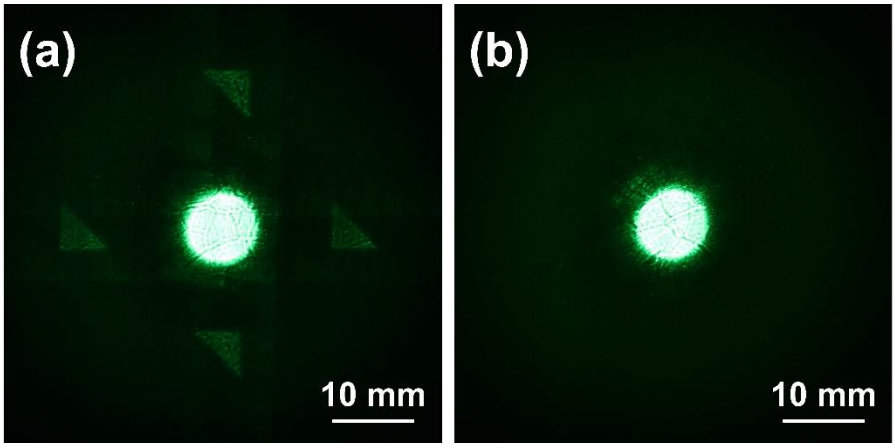

Figure S9. (a) Diffraction pattern of an optical device with strip-shaped structural arrays. (b) Diffraction pattern of an optical device processed with laser pulse energies lower than the formation of bulges and ablated regions.

Figure S9a shows the diffraction pattern of the device in **Figure S1a**. The device consists of two triangular regions with periodic strip-shaped structures parallel to x- and y-axes. The device projects triangular patterns onto the screen owing to diffraction effects. The same pattern

was processed using ultrafast laser pulses with energy just lower than that required for the formation of bulges and ablated regions. The diffraction pattern was shown in **Figure S9b**, and no diffraction effect was observed on the silk film with different exposure times for the camera. The diffraction pattern in **Figure S9b** is the same as the unprocessed silk film.

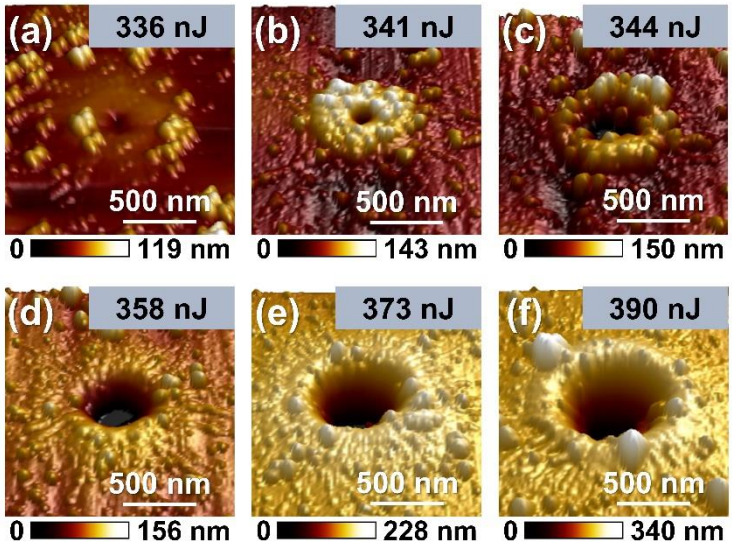

Figure S10. AFM images of craters processed using laser pulses with pulse energies ranging from 336 to 390 nJ.

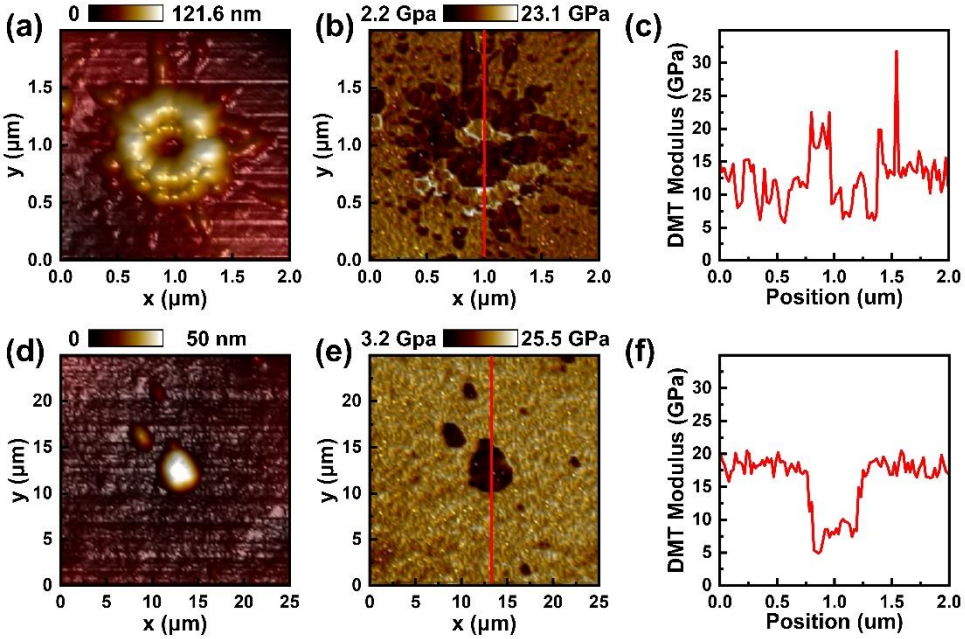

Figure S11. Topography and DMT modulus maps of (a-c) a crater, and (d-f) a bulge.

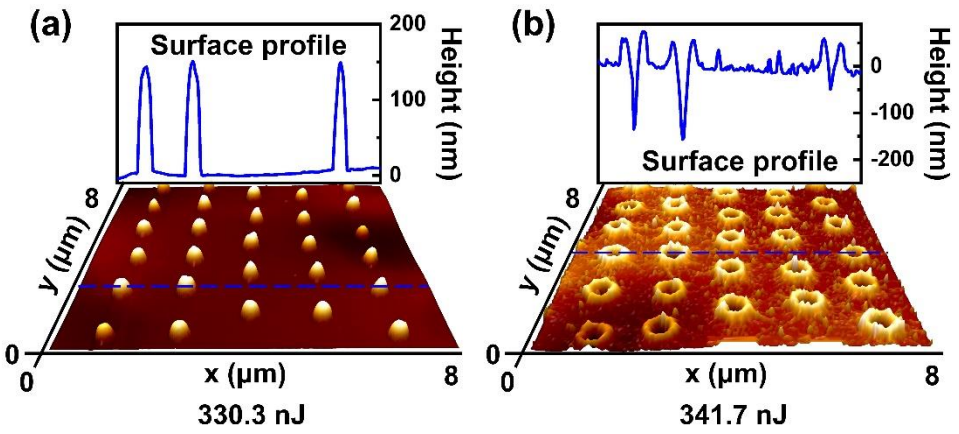

Figure S12. (a) AFM image and cross-sectional profile of a bulge array processed by ultrafast laser pulses with pulse energy of 330.3 nJ. (b) AFM image and cross-sectional profile of a crater array processed by ultrafast laser pulses with pulse energy of 341.7 nJ.

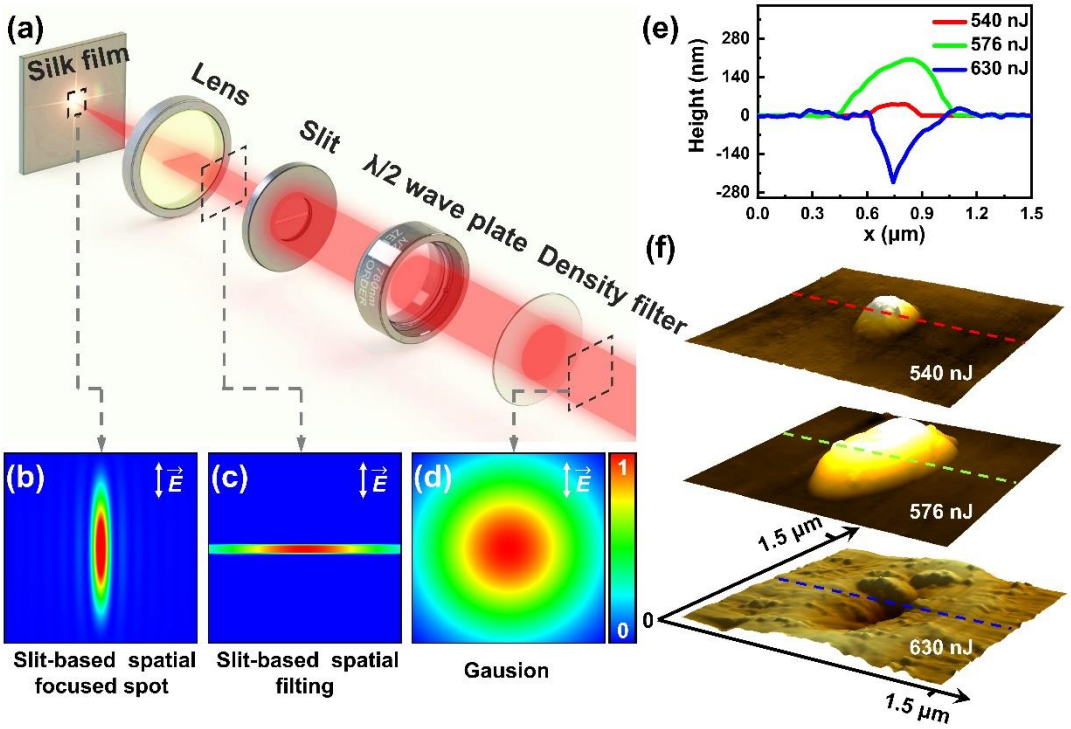

Figure S13. (a) The optical setup of the slit-based spatial light shaping. The simulated intensity profiles in the planes (b) at the focal, (c) after passing through the slit, and (d) in front of the slit. (e) The cross-sectional profiles and (f) AFM images of strip-shaped structures processed using reshaped ultrafast laser pulses.

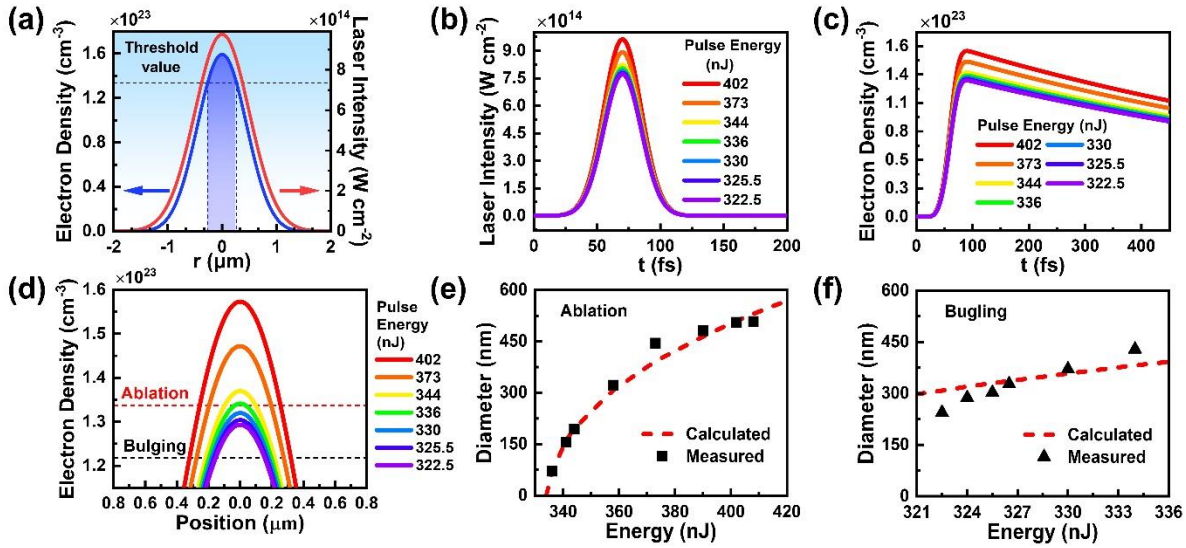

Figure S14. (a) Spatial distribution of laser intensity and corresponding free electron density. (b) Laser intensity, (c) calculated electron density, (d) spatial distribution of maximum electron density of the silk film with pulse energy ranging from 322.5 ~ 402 nJ. The measured and calculated diameters of (e) the craters and (f) the bulges processed with different pulse energies.

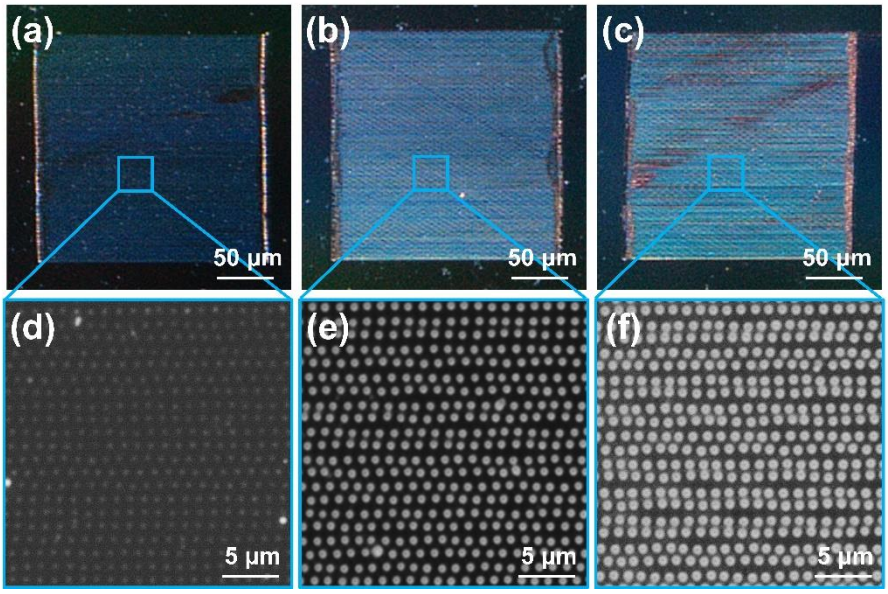

Figure S15. Dark-field optical micrographs of microstructures with different sizes but the same center-to-center distance (1.2 μm).

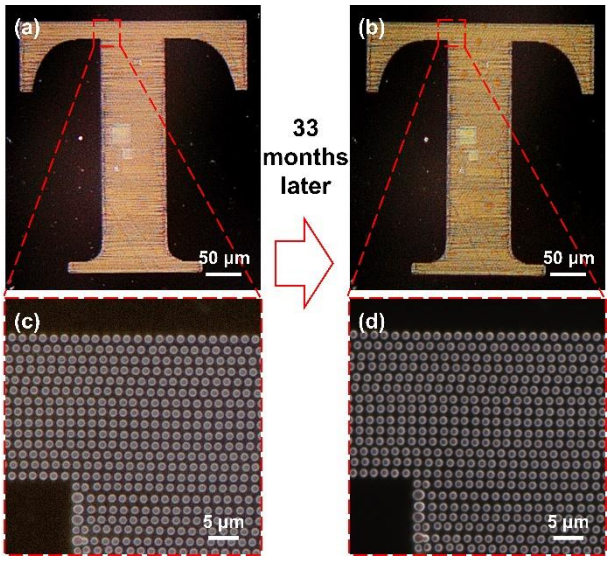

Figure S16. Long-term stability. (a-b) Dark-field optical micrograph of a pattern of "T". (c-d) Partially magnified optical micrograph images of microstructural arrays.

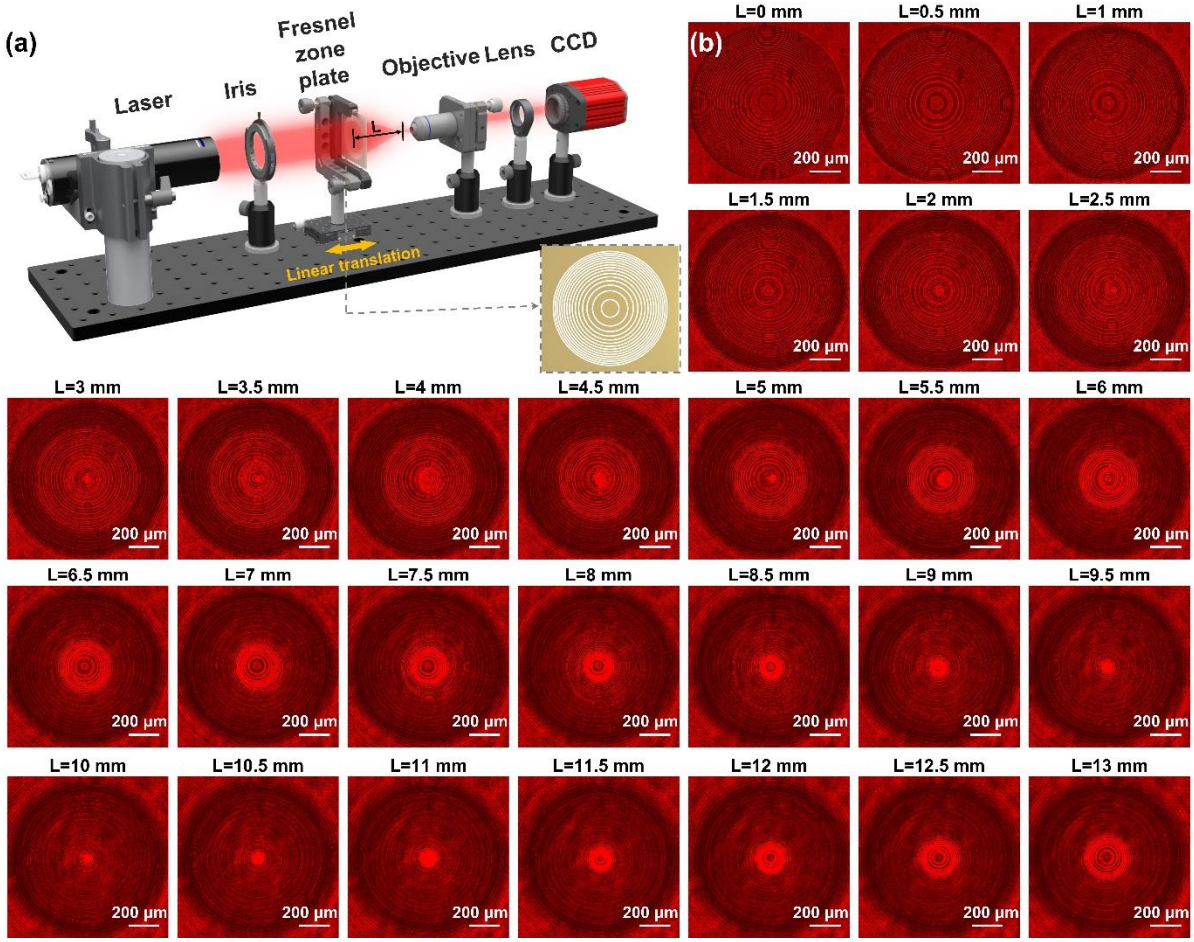

Figure S17. (a) The experimental setup for the optical testing of the Fresnel zone plate. (b) Measured distribution of light field intensity behind the Fresnel zone plate.

Table S1. Atomic concentration table of silk film before and after processing by ultrafast laser with power ranging from 1.05 mW to 1.51 mW.

Atomic Concentration	**C 1s**	**O 1s**	**N 1s**
Native	58.39	36.68	4.93
1.05 mW	60.43	33.41	5.14
1.13 mW	61.63	32.94	5.43
1.22 mW	62.08	31.08	6.80
1.31 mW	64.13	28.5	6.81
1.41 mW	63.86	27.96	8.18
1.51 mW	64.03	27.88	8.09

Table S2. Comparison of our method with other fabrication techniques for silk film processing.

Method	Morphology	Minimum diameter / width	Template, mask, or probe	Processing environment	References
Ion beam lithography	**Crater & Bulge**	13.2 nm	**No**	Vacuum	1
Electrons beam lithography	Bulge	14.8 nm	**No**	Vacuum	2
Electrons beam lithography	**Crater & Bulge**	30 nm	**No**	Vacuum	3
Near-field nanolithography	**Crater & Bulge**	Bulge: 35 nm	Yes	**In air**	4
Ultrafast laser direct writing	**Crater & Bulge**	**Crater: 71 nm Bulge: 244 nm**	**No**	**In air**	**This work**
Template-assisted patterning	**Crater & Bulge**	100 nm	Yes	**In air**	5
Nanoimprinting	Crater	200 nm	Yes	**In air**	6
Self-assembly	Crater	240 nm	Yes	**In air**	7
Ultraviolet lithography	Bulge	1 μm	Yes	**In air**	8
Template-assisted patterning	**Crater & Bulge**	2 μm	Yes	**In air**	9

Ultrafast laser direct writing	**Crater & Bulge**	2 μm	**No**	**In air**	10
Inkjet printing	Bulge	5 μm	**No**	**In air**	11
Ultraviolet lithography	Bulge	10 μm	Yes	**In air**	12
Inkjet printing	**Crater & Bulge**	30 μm	**No**	**In air**	13

Movie S1 (separate file). A silk film-based optical encryption device. The square-shaped device was fixed to a rack and illuminated with a 530 nm laser.

References

1 J Jiang, S Zhang, Z Qian *et al.* Protein Bricks: 2D and 3D Bio-Nanostructures with Shape and Function on Demand. *Advanced Materials* **30**, 1705919 (2018).

2 N Qin, Z-G Qian, C Zhou *et al.* 3D electron-beam writing at sub-15 nm resolution using spider silk as a resist. *Nature Communications* **12**, 5133 (2021).

3 S Kim, B Marelli, M A Brenckle *et al.* All-water-based electron-beam lithography using silk as a resist. *Nature Nanotechnology* **9**, 306-310 (2014).

4 W Lee, Z Zhou, X Chen *et al.* A rewritable optical storage medium of silk proteins using near-field nano-optics. *Nature Nanotechnology* **15**, 941-947 (2020).

5 H Perry, A Gopinath, D L Kaplan *et al.* Nano- and micropatterning of optically transparent, mechanically robust, biocompatible silk fibroin films. *Advanced Materials* **20**, 3070-3072 (2008).

6 J J Amsden, P Domachuk, A Gopinath *et al.* Rapid Nanoimprinting of Silk Fibroin Films for Biophotonic Applications. *Advanced Materials* **22**, 1746-+ (2010).

7 Y Y Diao, X Y Liu, G W Toh *et al.* Multiple Structural Coloring of Silk-Fibroin Photonic Crystals and Humidity-Responsive Color Sensing. *Advanced Functional Materials* **23**, 5373-5380 (2013).

8 N E Kurland, T Dey, S C Kundu *et al.* Precise Patterning of Silk Microstructures Using Photolithography. *Advanced Materials* **25**, 6207-6212 (2013).

9 Z Zhou, Z Shi, X Cai *et al.* The Use of Functionalized Silk Fibroin Films as a Platform for Optical Diffraction-Based Sensing Applications. *Advanced Materials* **29** (2017).

10 K Maximova, X Wang, A Balcytis *et al.* Silk patterns made by direct femtosecond laser writing. *Biomicrofluidics* **10** (2016).

11 S T Parker, P Domachuk, J Amsden *et al.* Biocompatible Silk Printed Optical Waveguides. *Advanced Materials* **21**, 2411-+ (2009).

12 N E Kurland, T Dey, C Wang *et al.* Silk Protein Lithography as a Route to Fabricate Sericin Microarchitectures. *Advanced Materials* **26**, 4431-4437 (2014).

13 W Li, Y Wang, M Li *et al.* Inkjet Printing of Patterned, Multispectral, and Biocompatible Photonic Crystals. *Advanced Materials* **31**, 1901036 (2019).